

# X-ray and optical spectroscopic study of a $\gamma$ Cassiopeiae analog source $\pi$ Aquarii

Masahiro TSUJIMOTO,<sup>1</sup> Takayuki HAYASHI,<sup>2</sup> Kumiko MORIHANA,<sup>3</sup>  
Yuki MORITANI<sup>3</sup>

<sup>1</sup>Japan Aerospace Exploration Agency, Institute of Space and Astronautical Science,  
Chuo-ku, Sagami-hara, Kanagawa 252-5210, Japan

<sup>2</sup>NASA's Goddard Space Flight Center, Greenbelt, MD 20771, USA

<sup>3</sup>Subaru Telescope, National Astronomical Observatory of Japan, Hilo, HI 96720, USA

\*E-mail: tsujimot@astro.isas.jaxa.jp

Received ; Accepted

## Abstract

$\gamma$  Cas analog sources are a subset of Be stars that emit intense and hard X-ray emission. Two competing ideas for their X-ray production mechanism are (a) the magnetic activities of the Be star and its disk and (b) the accretion from the Be star to an unidentified compact object. Among such sources,  $\pi$  Aqr plays a pivotal role as it is one of the only two spectroscopic binaries observed for many orbital cycles and one of the three sources with X-ray brightness sufficient for detailed X-ray spectroscopy. Bjorkman et al. (2002) estimated the secondary mass  $>2.0 M_{\odot}$  with optical spectroscopy, which would argue against the compact object being a white dwarf (WD). However, their dynamical mass solution is inconsistent with an evolutionary solution and their radial velocity measurement is inconsistent with later work by Nazé et al. (2019). We revisit this issue by adding a new data set with the NuSTAR X-ray observatory and the HIDES échelle spectrograph. We found that the radial velocity amplitude is consistent with Nazé et al. (2019), which is only a half of that claimed by Bjorkman et al. (2002). Fixing the radial velocity amplitude of the primary, the secondary mass is estimated as  $<1.4 M_{\odot}$  over an assumed range of the primary mass and the inclination angle. We further constrained the inclination angle and the secondary mass independently by fitting the X-ray spectra with a non-magnetic or magnetic accreting WD model under the assumption that the secondary is indeed a WD. The two results match well. We thus argue that the possibility of the secondary being a WD should not be excluded for  $\pi$  Aqr.

**Key words:** stars: individual ( $\pi$  Aqr) — stars: emission-line, Be — stars: white dwarfs — X-rays: stars

## 1 Introduction

$\gamma$  Cas analog sources are a subset of Be stars that emit intense and hard X-ray emission distinctive from other Be-type stars (Berghoefer et al. 1997). The X-ray luminosity is  $10^{32}$ – $10^{33}$  erg s<sup>−1</sup> and the emission extends beyond 10 keV. The cause for such X-ray emission remains a puzzle for more than four decades. Two competing ideas for producing the X-ray emitting plasma are (a) the magnetic activities of the Be star

and its disk (Robinson & Smith 2000; Smith et al. 2004) and (b) the accretion from the Be star to an unidentified compact object. The compact object is either a white dwarf (WD; Haberl 1995; Kubo et al. 1998; Hamaguchi et al. 2016) or a neutron star (NS; White et al. 1982; Postnov et al. 2017). More details can be found in Smith et al. (2016) for the review and in a conference site in 2018<sup>1</sup> for more recent developments and related

<sup>1</sup> Materials available at <https://gammacas-enigma.sciencesconf.org/>.

topics.

Since the X-ray detection from the prototypical  $\gamma$  Cas (Mason et al. 1976), the number of  $\gamma$  Cas analog sources has increased to a few dozens thanks mostly to the recent X-ray surveys using XMM-Newton observatory (Motch et al. 2010; Nazé et al. 2020). The increase will be accelerated with eROSITA (Merloni et al. 2012) in the near future.  $\pi$  Aqr is one of the recent addition to the group (Nazé et al. 2017). This source may play a pivotal role in solving the long-standing puzzle of the X-ray production mechanism of  $\gamma$  Cas analog sources for its unique features. First, it is one of a few, along with  $\gamma$  Cas and HD 110432 (BZ Cru), that are bright enough in X-ray flux to allow detailed X-ray spectroscopy with modern instruments. Second, it is one of the two, along with  $\gamma$  Cas, that are known to be a binary with optical spectroscopy covering many orbital cycles. Note that Nazé et al. (2022) revealed the spectroscopic binary nature of six more  $\gamma$  Cas analogs. Third, the source was observed both in the normal B and Be phases. It is common that Be stars make transitions between the two phases due to the formation and the destruction of the circumstellar disks and shells, but  $\pi$  Aqr is the only one that exhibited this transition among  $\gamma$  Cas analog sources to date.

Bjorkman et al. (2002) discovered the spectroscopic binary nature of this source. They monitored the  $H\alpha$  profile between 1996 and 2001 when  $\pi$  Aqr was in the normal B star phase. Both emission and absorption lines were detected, which changed their radial velocity sinusoidally in the opposite phase. They argued that the absorption is from the primary B star and the emission is from the unknown secondary. The claimed mass for the primary and the secondary are, respectively,  $M_1 \sin i = 12.4 M_\odot$  and  $M_2 \sin i = 2.0 M_\odot$ , where  $i$  is the orbital inclination angle. This apparently excludes the possibility that the secondary is a WD beyond the Chandrasekhar mass limit of  $1.38 M_\odot$ . However, the following studies (Zharikov et al. 2013; Nazé et al. 2019) pointed out some inconsistencies in this orbital solution.

The purpose of this paper is to revisit the mass estimate of the secondary with new sets of data both in the X-ray and optical spectroscopy. For  $\gamma$  Cas and HD 110432, it was demonstrated that the secondary mass can be constrained, independently from optical measurements, by fitting the broad-band (0.5–50 keV) X-ray spectra with a physically motivated model if the WD scenario is adopted as a working hypothesis (Tsujimoto et al. 2018). The two independent mass estimates by the optical and X-ray spectroscopy were consistent with each other for  $\gamma$  Cas, which is a spectroscopic binary. We apply this approach to  $\pi$  Aqr.

A comprehensive study of  $\pi$  Aqr was made by Nazé et al. (2019) with a year-long monitoring in the 2018 season using both the Neil Gehrels Swift Observatory in the X-rays below 10 keV and the échelle spectrograph mounted at the 1.2 m

TIGRE telescope in the optical. We supplement their work in the 2019 season by adding the data with the NuSTAR observatory in the X-rays above 10 keV and the échelle spectrograph mounted at the 1.88 m telescope in the Okayama Astrophysical Observatory (OAO).

The outline of this paper is as follows. In § 2, we present the NuSTAR X-ray (§ 2.1) and the OAO optical (§ 2.3) data sets. To complement the soft X-ray band spectrum, we also use the archived XMM-Newton data (§ 2.2; the same data presented in Nazé et al. 2017). In § 3, we present the analysis of the X-ray (§ 3.1) and optical (§ 3.2) spectra separately. In § 4, we revisit the secondary mass estimate based on the literature and examine consistency with our result. We will argue for a lower mass estimate for the secondary than was originally proposed.

We adopt the following parameters for  $\pi$  Aqr. The distance is 286 pc based on a Gaia parallax measurement (Prusti et al. 2016; Brown et al. 2018). The binary orbit is 84.1 day with the orbital phase  $\phi_{\text{orb}} = 0$  at the heliocentric Julian date of 2450275.5. The ephemeris was derived spectroscopically in 1996–2000 (Bjorkman et al. 2002) and was confirmed stable in 2018 (Nazé et al. 2019). The effective temperature of the primary is  $T_{\text{eff}} = 24 \pm 1$  kK and the visual extinction is  $A_V = 0.15$  mag based on the SED during a normal B star phase (Bjorkman et al. 2002).

## 2 Observations and Data Reduction

### 2.1 NuSTAR

We observed  $\pi$  Aqr with the Nuclear Spectroscopic Telescope Array (NuSTAR; Harrison et al. 2013) on 2019 November 4–5 for a 54 ks exposure with an observation identification number 30501009002. NuSTAR is a space-born X-ray telescope with a wide-band coverage in the 3–79 keV band. Above  $\sim 10$  keV, in particular, the telescope has better sensitivity than previous telescopes by two orders of magnitude thanks to the focusing mirrors employed in this energy band for the first time.

Two focal plane module (FPM) instruments are placed at the focus of two telescopes, which are called FPMA and FPMB. Each module carries an array of CdZnTe pixel detectors surrounded by the CsI anti-coincidence detectors. The array covers a  $12'0$  field with a telescope half-power diameter of  $1'0$ . The energy resolution is modest of 400–900 eV in the 10–70 keV range. These features make this telescope uniquely suited for our present study, in which X-ray spectral curvature above 10 keV is a key to understanding the nature of the source.

We started from the X-ray cleaned event list produced by the standard pipeline tool `nupipeline` version 0.4.6. No other X-ray source was found in the image. We extracted source events from a circle of a  $3'$  radius and background events from an annulus of  $4'–6'$  concentric to the source. The resultant source

and background (normalized to the extraction area) count rates were 1.1 and 0.16 s<sup>-1</sup> respectively when the two instruments are combined.

The light curve is shown in figure 1. On one hand, the count rate of events in the 1.4–76.3 keV band shows an increasing trend with some variability throughout the observation. On the other hand, the spectral hardness defined by  $(H - S)/(H + S)$  is constant, where  $H$  and  $S$  are the count rates hard- and soft-ward of the median energy of all events (5.4 keV). We thus consider that there is no change in the spectral shape besides the flux and construct spectrum without dividing by time.

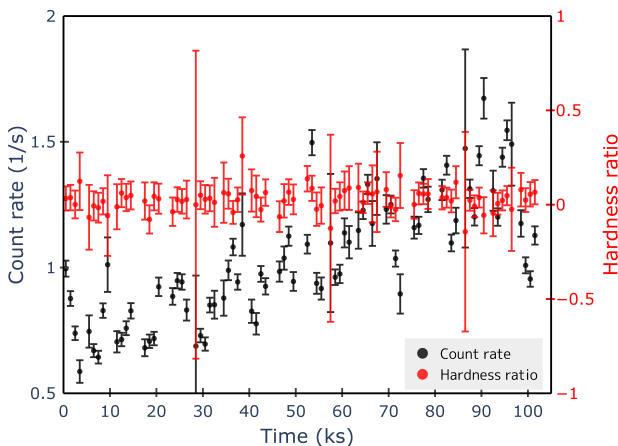


**Fig. 1.** Count rate (1.4–76.3 keV) and hardness ratio  $((H - S)/(H + S))$ , where  $S$  and  $H$  are count rates of 1.4–5.4 and 5.4–76.2 keV, respectively) binned by 1 ks of the NuSTAR FPMA and FPMB combined.

We made background subtracted spectra separately for FPMA and FPMB. The auxiliary response files (ARF) of the telescope as well as the redistribution matrix functions (RMF) of the instruments were produced by the `nuproducts` version om.3.0. Figure 2 shows the spectra.

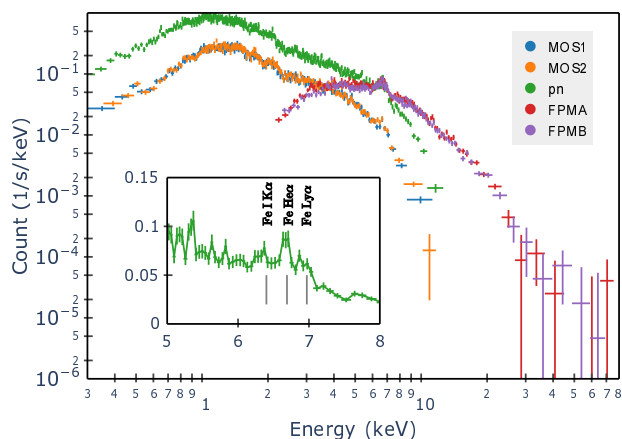


**Fig. 2.** Spectra of EPIC MOS1, MOS2, pn and NuSTAR FPMA and FPMB. The inset gives an enlarged view in the Fe K band of the EPIC pn spectrum.

## 2.2 XMM-Newton

We retrieved the archival data of  $\pi$  Aqr observed with XMM-Newton. This is to complement the X-ray data down to 0.3 keV and to have a better energy resolution than NuSTAR at the Fe K band in the 6–7 keV to resolve the prominent three emission lines of the Fe XXV Ly $\alpha$  and Fe XXIV He $\alpha$  lines from high-temperature plasma as well as the Fe fluorescence line as a re-processed product of it. The observation with an identification number 0720390701 was made on 2013 November 16–17 for a 52 ks exposure. The details of the observations and the results can be found in Nazé et al. (2017).

We used the data taken with the European Photon Imaging Camera (EPIC) equipped with two MOS cameras (Turner et al. 2001) and one pn camera (Strüder et al. 2001). After the standard pipeline processing using the `emchain` and `epchain` tools in the SAS package version 17.0, we removed events taken during high background or those having a pixel distribution pattern of non X-ray events. We extracted source events from a circle of a 30'' radius and background events from an annulus of 75''–90'' concentric to the source.

As described in Nazé et al. (2017), the count rate varied by a factor of  $\sim 3$  while the hardness ratio was constant, similarly to the NuSTAR data (§ 2.1). We thus constructed spectra by integrating the entire observation. The ARF and RMF were generated using the standard tools in the SAS package. Figure 2 shows the spectra.

## 2.3 OAO

We observed  $\pi$  Aqr 13 times from 2019-09-06 to 2019-12-23 using the High Dispersion Echelle Spectrograph (HIDES) placed at the coudé focus of the 188 cm telescope in the Okayama Astronomical Observatory (OAO). The OAO is no longer supported by the National Astronomical Observatory of Japan (NAOJ) as a common-use facility open to the community, but it continues operation under the contract among NAOJ, Tokyo Institute of Technology, and Asakuchi City. HIDES is an échelle spectrograph equipped with a mosaic of three 2k×4k CCD cameras covering a wide range of 3800–7500 Å. A fiber link is used between the telescope and HIDES to improve optical throughput while keeping the radial velocity precision to a few km s<sup>-1</sup> at a resolution of  $>50,000$  (Kambe et al. 2013).

Table 1 shows the observation log. The planned cadence was once per week, which was randomized to some extent due to weather and facility issues. Figure 3 (a) shows the light curve for the last ten years taken with an automated sky monitor (Maehara 2013).  $\pi$  Aqr exhibits a long-term variability in this time scale in comparison to a nearby field star  $\xi$  Aqr. During our OAO observation campaign, the star was relatively stable in the V-band magnitude. Figure 3 (b) shows a close-up view of the 2019 season. Variability within the season is presumably due to

systematics as similar variation is also seen in the reference star. A total of 13 OAO observations cover 1.28 orbital cycles of  $\pi$  Aqr. The seventh observation was executed during the NuSTAR observation unintentionally due to unrelated schedule changes in both observatories.

Each observation has a mean exposure time and air mass respectively of 18.5 min and 1.4. We took bias and flat data before and after observations every night, and comparison data with a ThAr lamp. We used pipeline products, in which the bias was subtracted, the échelle orders were traced, scattering and cosmic-rays were removed, the image flatness was corrected, one-dimensional spectra were extracted, wavelengths were registered, and continuum was corrected for flatness. Between the 10'th and 11'th observations, a small earthquake of a magnitude of 3 hit the observatory on 2019 November 26, which made some shifts in the optical alignment of the instrument. The échelle orders changed for some features as a result, but no systematic difference was found in the registered wavelengths. The typical uncertainty of the wavelength is estimated as  $\sim 0.03$  Å from telluric features.

**Table 1.** Observation log

Num	Date	Time* (UT)	$t_{\text{exp}}^{\dagger}$ (s)	Air mass*	$\phi_{\text{orb}}^{\ddagger}$
1	2019-09-06	11:25:08	1115	1.72	0.56
2	2019-09-13	10:52:54	1128	1.76	0.65
3	2019-09-24	16:45:51	1200	1.91	0.78
4	2019-10-08	10:06:07	1166	1.45	0.95
5	2019-10-14	10:32:55	1098	1.29	0.02
6	2019-10-22	12:27:00	1065	1.23	0.11
7 <sup>§</sup>	2019-11-05	09:11:50	1095	1.28	0.28
8	2019-11-09	09:24:16	1076	1.23	0.33
9	2019-11-14	08:51:32	1083	1.25	0.39
10	2019-11-19	09:11:23	1064	1.20	0.44
11	2019-12-07	08:44:33	1058	1.20	0.66
12	2019-12-11	08:49:17	1060	1.21	0.71
13	2019-12-23	10:43:29	1203	1.82	0.85

\* Mean value in the exposure.

<sup>†</sup> Exposure time.

<sup>‡</sup> Orbital phase based on the ephemeris by Bjorkman et al. (2002).

<sup>§</sup> Simultaneous with the NuSTAR observation.

### 3 Analysis

#### 3.1 X-ray spectra

Figure 2 shows the spectra of XMM-Newton EPIC and NuSTAR FPM. As commonly seen in all  $\gamma$  Cas analog sources, the X-ray spectrum of  $\pi$  Aqr is also characterized by a hard continuum extending up to 50 keV, and the Fe K complex with the quasi-neutral Fe I K $\alpha$  line at 6.4 keV as well as the highly-ionized Fe XXV He $\alpha$  line at 6.7 keV and Fe XXVI Ly $\alpha$  line at 7.0 keV as shown in the inset.

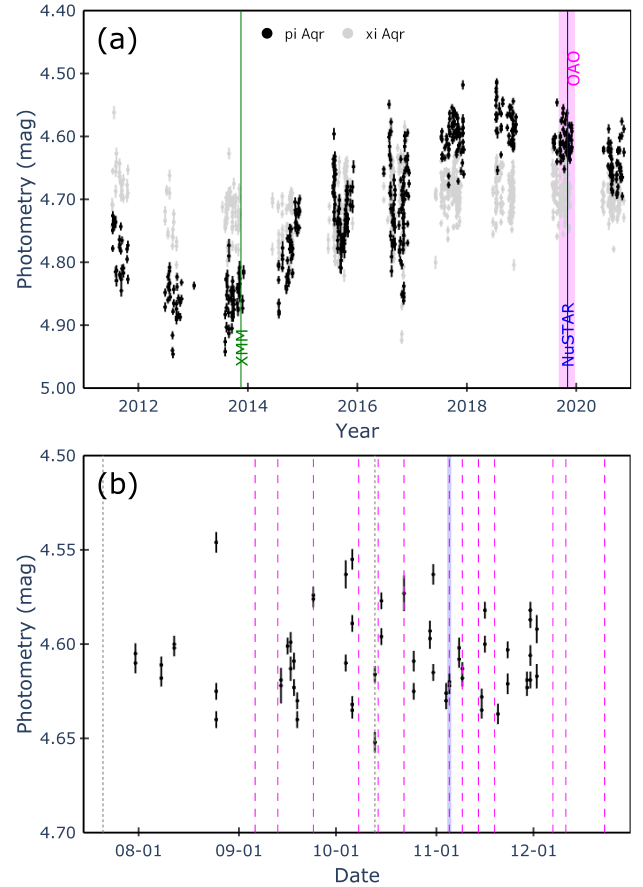


**Fig. 3.** (a) Decadal V-band light curve of  $\pi$  Aqr and its near-by A0V star  $\xi$  Aqr for reference taken with the Kamogata/Kiso/Kyoto Wide-field Survey (Maehara 2013). The epochs of the data presented in this paper is given in colors. (b) Close-up view of the 2019 season. The epochs of each OAO observation and the duration of the NuSTAR observation are shown with colors. Two dashed lines indicate the epoch of  $\phi_{\text{orb}} = 0$  based on the ephemeris by Bjorkman et al. (2002).

We apply two accreting WD models —non-magnetic (§ 3.1.1) and magnetic (§ 3.1.2)— to  $\pi$  Aqr as was done for  $\gamma$  Cas and HD 110432 (Tsujiimoto et al. 2018). We have no clue if  $\pi$  Aqr, or any  $\gamma$  Cas analog sources, host a non-magnetic or magnetic WD, thus we need to test both possibilities, which require different models.

All the XMM-Newton EPIC and the NuSTAR FPM spectra (figure 1) were fitted simultaneously. The source is known to be variable in the X-rays through a year-long monitor using the Neil Gehrels Swift Observatory (Nazé et al. 2019), hence we allowed the normalization of the NuSTAR spectra to be different from that of the XMM-Newton spectra. The hydrogen-equivalent column density ( $N_{\text{H}}$ ) also varies (Nazé et al. 2019), but because the extinction is too low to affect the hard band X-ray spectra of the NuSTAR data, we kept it to be the same between the XMM-Newton and NuSTAR models. The value of  $N_{\text{H}}$  due to the interstellar matter is fixed to  $3.16 \times 10^{21} \text{ cm}^{-2}$  derived from two consistent measurements of  $A_V = 0.15 \text{ mag}$



(Bjorkman et al. 2002) and  $E(B - V) = 0.07$  mag (Jenkins 2009) and an additional local extinction was derived by the fitting.

### 3.1.1 Non-magnetic accreting WD model

Non-magnetic accreting WDs have magnetic fields ( $<0.1$  MG) that are not strong enough to disturb the accretion from the companion star. They are known as copious X-ray sources (Mukai 2017). The X-ray emission comes from the boundary layer (Patterson & Raymond 1985), in which the gravitational energy released through accretion is dissipated into heat by the friction with the slowly rotating surface of the WD.

The X-ray spectra at quiescence are well modeled by the cooling flow model (Pandel et al. 2005; Wada et al. 2017), which is a convolution of the single temperature plasma at a collisional ionization equilibrium and the isobaric temperature gradient. In addition, non-magnetic accreting WDs often show partial covering absorber local to the star and the fluorescent and scattered emission reprocessed at the WD surface and the accretion disk.

We fitted the observed spectra first with the `mkcflow` model (Mushotzky & Szymkowiak 1988) attenuated by the `tbabs` model (Wilms et al. 2000) for the interstellar absorption. The free parameters are the maximum temperature of the temperature gradient ( $T_{\max}$ ), the mass accretion rate ( $\dot{M}_X$ ), and the metallicity of the plasma ( $Z$ ) relative to the ISM value (Wilms et al. 2000). We fixed the minimum temperature of the cooling flow to the lowest available value (80 eV). We also made the NuSTAR flux relative to XMM-Newton as a free parameter.

This yielded an unsatisfactory fit with large residuals at (a) the soft-band end, (b) the hard-band end, and (c) 6.4 keV. To account for these deviations, we modified the model by (a) convolving with a partial covering model and (b) the Compton reflection model (Magdziarz et al. 1995) and by (c) adding a Gaussian model. The additional free parameters are (a) absorption column ( $N_H$ ) and the covering fraction in the partial covering model, (b) the subtended angle for the Compton reflection ( $d\Omega/2\pi$ ), and (c) the intensity of the 6.4 keV line represented by a Gaussian distribution with the center and the intrinsic width fixed at 6.40 keV and 0 eV. The fluorescence and the Compton scattering are two competing processes in the reprocessed emission under the same geometry. No model has been developed to explain both, thus we took the following approach. Based on George & Fabian (1991), we derived  $d\Omega/2\pi$  from the equivalent width ( $EW_{\text{Fe}}$ ) of the 6.4 keV line and compared it to the one derived for the Compton scattering. We iterated the fitting until the two converged for an assumed reflection angle  $i_r$ . We obtained a reasonable fitting result for several selected values in the range  $i_r = 50$ –60 degrees that cover the conceivable range (see § 4.2) with little difference in the fitting parameters other than  $d\Omega/2\pi$ . Table 2 and figure 4 show the result for  $i_r = 60$  de-

gree.

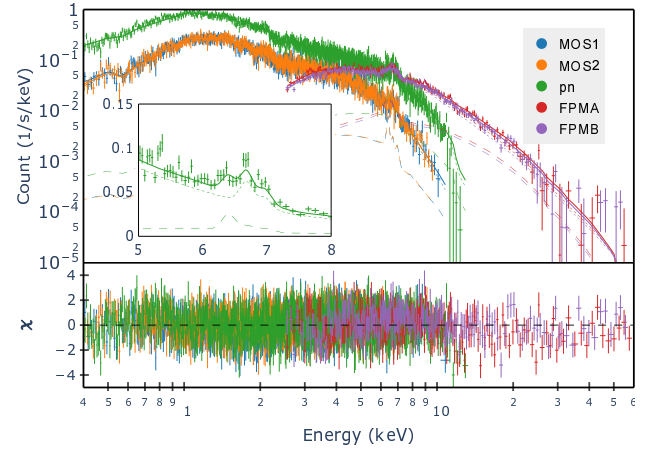


**Fig. 4.** Spectrum and the best-fit non-magnetic accreting WD model. The upper panels show the data (plus marks) and the model (dotted, dashed, and solid curves respectively for the direct, reprocessed, and total components), whereas the bottom panel shows the residuals to the fit. The inset gives an enlarged view in the Fe K band of the EPIC pn spectrum.

**Table 2.** Best-fit parameters with the non-magnetic accreting WD model\*.

Model	Parameter	$\pi$ Aqr
(Fixed values)		
Distance	$D$ (pc)	286
Reflection angle	$i_r$ (degree)	60
<code>tbabs</code>	$N_H$ ( $10^{21} \text{ cm}^{-2}$ )	3.16
(Fitted values*)		
<code>tbpcf</code>	$N_H$ ( $10^{22} \text{ cm}^{-2}$ )	$0.53 \pm 0.02$
	Covering fraction	$0.79 \pm 0.01$
<code>mkcflow</code>	$T_{\max}$ (keV)	$19.1^{+0.29}_{-0.37}$
	$Z$ (solar)	$0.51 \pm 0.03$
	$\dot{M}_X$ ( $10^{-11} M_{\odot} \text{ yr}^{-1}$ )	$3.15^{+0.04}_{-0.03}$
<code>reflect</code>	$d\Omega/2\pi$	0.79
<code>gauss</code>	$EW_{\text{Fe}}$ (eV)	$68 \pm 8$
<code>const</code>	NuSTAR/XMM flux	$2.26 \pm 0.02$
$\chi^2_{\text{red}}$ (d.o.f.)		1.04 (3350)

\* The errors indicate a  $1\sigma$  statistical uncertainty.

### 3.1.2 Magnetic accreting WD model

Next, we try fitting the spectra with a magnetic accreting WD model. In magnetic WDs, the accretion disk is truncated and the matter accretes along the magnetic field to form an accretion column above the magnetic poles. A strong shock is formed above the WD surface, where the infalling kinetic energy is dissipated into heat as the X-ray emitting plasma.

X-ray spectra can be synthesized by calculating the temperature and pressure gradient along the column and adding the

emission from them. We used the *acrad* model (Hayashi et al. 2021), in which the X-ray spectra are calculated by solving the plasma fluid equations along the dipole magnetic field as a function of the WD mass ( $M_{\text{WD}}$ ) and the specific mass accretion rate, or the mass accretion rate per unit area ( $a$ ). This model further calculates the reprocessed emission. The reprocessing takes place at the WD surface either by fluorescence or by Compton scattering. The 6.4 keV emission line and the Compton reflection components are included in the model as a function of the reflection angle ( $i_r$ ). These parameters as well as the metal abundance ( $Z$ ) are constrained by the spectral fitting. Similarly to the non-magnetic WD case (§ 3.1.1), we attenuated the *acrad* model with the *tbabs* (Wilms et al. 2000) for the interstellar absorption and *tbpcf* for the local partial absorption. The fitting was successful with reasonable values of the best-fit parameters (table 3 and figure 5).

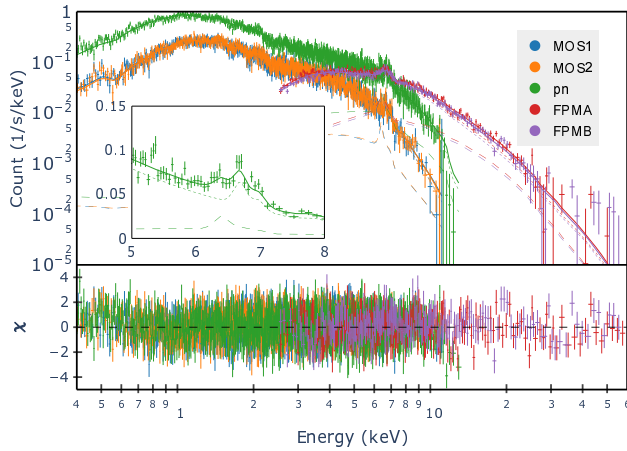


**Fig. 5.** Spectrum and the best-fit magnetic accreting WD model. The symbols follow figure 4.

### 3.2 Optical spectra

The optical spectra have numerous features. Figure 6 shows the local spectra of noticeable features of H, He, and some metals laid out along the date of observations.  $H\alpha$  profile appears single-peaked emission,  $\text{HeI}\lambda 4472$  single-peaked absorption, and the others double-peaked emission. Fixed wavelengths modulated by the Doppler shift of the Earth's motion around the heliocenter ( $-2.6$  to  $-28.0 \text{ km s}^{-1}$  for the observation span) are shown with dotted curves to trace the peaks or valleys. The peaks and valleys are fluctuating around the curve collectively with the orbital period, suggesting that they are attributable to orbital motion.

To characterize the radial velocity changes, we used the  $H\alpha$  profile, which has the largest signal-to-noise ratio and references to compare to (Bjorkman et al. 2002; Nazé et al. 2019). We adopted the bisector method (Shafter et al. 1986), which has an advantage to avoid influences by the Be star activities

**Table 3.** Best-fit parameters with the magnetic accreting WD model\*.

Model	Parameter	$\pi \text{ Aqr}$
(Fixed values)		
Distance	$D$ (pc)	286
<i>tbabs</i>	$N_{\text{H}}$ ( $10^{21} \text{ cm}^{-2}$ )	3.16
(Fitted values*)		
<i>tbpcf</i>	$N_{\text{H}}$ ( $10^{22} \text{ cm}^{-2}$ )	$2.1 \pm 0.3$
	Covering fraction	$0.25 \pm 0.02$
<i>acrad</i>	$M_{\text{WD}}$ ( $M_{\odot}$ )	$0.51 \pm 0.01$
	$Z$ (solar <sup>†</sup> )	$0.26 \pm 0.02$
	$\log a$ ( $\text{g cm}^{-2} \text{ s}^{-1}$ )	$3.9^{+0.8}_{-3.8}$
	$i_r$ (degree)	$67^{+5}_{-7}$
<i>const</i>	NuSTAR/XMM flux	$2.18 \pm 0.03$
$\chi^2_{\text{red}}$ (d.o.f.)		1.00 (3349)

\* The errors indicate a  $1\sigma$  statistical uncertainty.

<sup>†</sup> Assuming that Fe represents the metals, the difference of the Fe abundance between the Anders & Grevesse (1989) and Wilms et al. (2000) is corrected to match with the latter.

(Moritani et al. 2018) and was adopted as one of the three methods in Nazé et al. (2019) that yielded consistent results. We removed the telluric absorption features and selected wavelengths of interest in the left- and right-hand side tails of a width of  $13 \text{ \AA}$  to cover about 40–10% of the peak values. Then, the left-hand side tail is reflected at a trial center wavelength and is correlated with the right-hand side tail. The center wavelength was derived by finding the maximum amplitude of the correlation among the trial center wavelengths. The correlation was fitted locally with a quadrature function, yielding a statistical error of  $\lesssim 0.1 \text{ km s}^{-1}$ .

The result is shown in the red dots in figure 7, which is consistent with Nazé et al. (2019) shown in the grey dots. We fitted the red dots with a sine curve having a fixed period of 84.1 day and constrained its amplitude of  $8.1 \pm 1.4 \text{ km s}^{-1}$  and its initial phase shift of  $-0.4 \pm 0.2$  radian. As discussed in Nazé et al. (2019), the radial amplitude is less than a half of the value reported in Bjorkman et al. (2002) as  $16.7 \text{ km s}^{-1}$ .

## 4 Discussion

### 4.1 Mass estimate with optical data

We revisit the mass estimate of the binary with the latest available literature. The mass of the binary constituents can be derived either by evolutionary or dynamical arguments. In  $\pi \text{ Aqr}$ , it is known that the two mass estimates contradict each other.

The evolutionary mass is estimated as follows. The effective temperature ( $T_{\text{eff}} = 24 \pm 1 \text{ kK}$ ) and the visual extinction ( $A_V = 0.15 \text{ mag}$ ) are derived from the SED fitting (Bjorkman

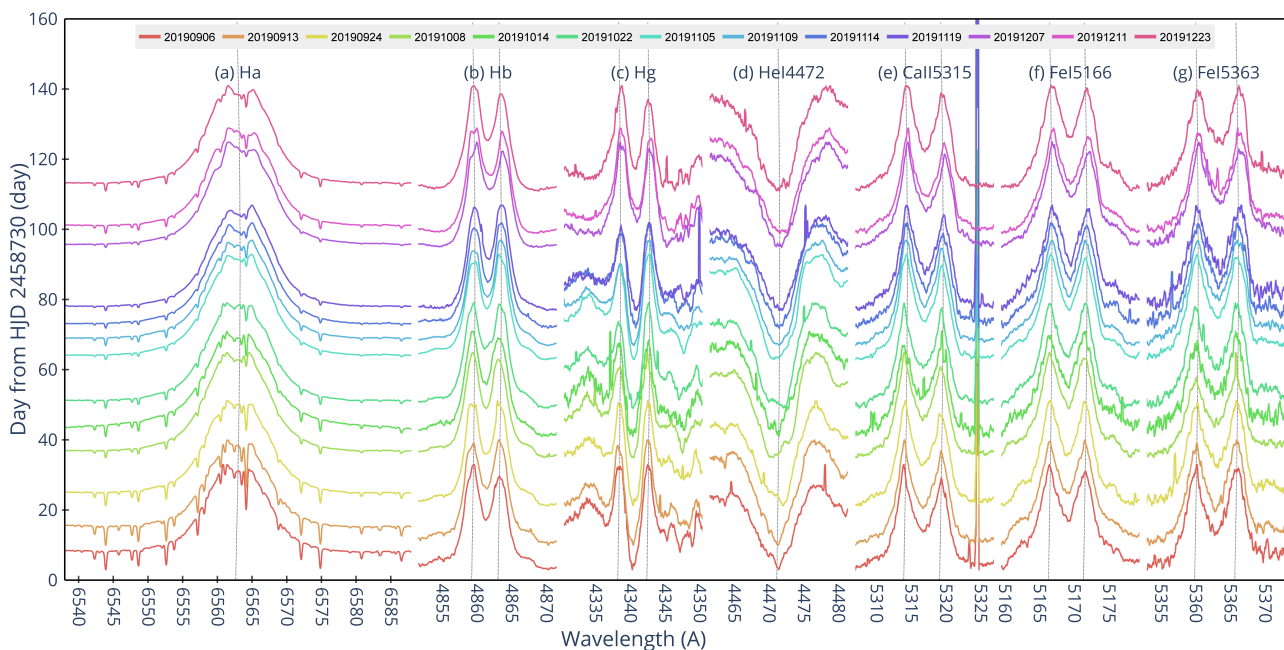


**Fig. 6.** Local spectra of some strong features shown with different colors for different observations. The features are detrended by subtracting the baseline and are normalized. The spectra are laid out along the observation dates. The width for  $H\alpha$  is 25 Å, while that for the others is 10 Å. The peaks and valleys are traced by the dotted curve showing a fixed wavelength modulated by the Earth's motion around the heliocenter.

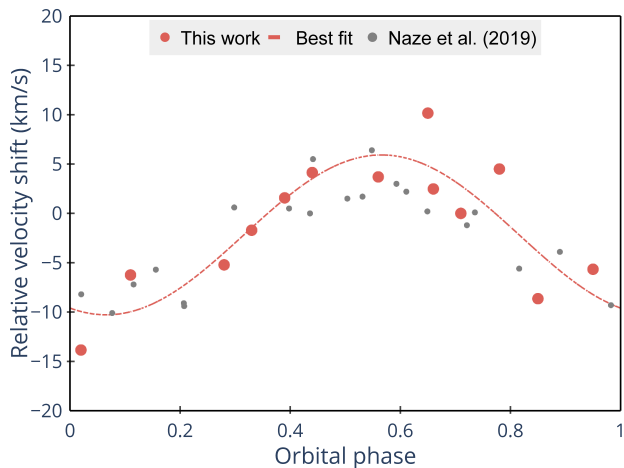


**Fig. 7.** Radial velocity relative to the mean as a function of phase. Red dots are by this work and red dashed curve is the best-fit sine curve. The grey dots are by Nazé et al. (2019).

et al. 2002). By applying the extinction and bolometric corrections to the observed brightness and by scaling with the distance, the absolute luminosity is obtained (Zharikov et al. 2013). We use the Gaia distance of 286 pc to obtain  $\log L/L_{\odot} = 3.87$ . Comparing  $T_{\text{eff}}$  and  $L$  to an evolutionary model (Ekström et al. 2012), the initial mass of the primary  $M_1 \sim 10 M_{\odot}$  is obtained.

The dynamical mass was estimated based on the spectra of the normal B phase (Bjorkman et al. 2002), in which they argued that the features from both constituents were observed;  $H\alpha$  absorption attributed to the primary with  $v_1 \sin i = 16.7 \pm$

$0.2 \text{ km s}^{-1}$  and the  $H\alpha$  emission attributed to the secondary with  $v_2 \sin i = 101.4 \pm 2 \text{ km s}^{-1}$ . From these, they derived  $M_1 \sin^3 i = 12.4 M_{\odot}$  and  $M_2 \sin^3 i = 2.0 M_{\odot}$  with a mass ratio of  $q = M_2/M_1 = 0.16$ .

Zharikov et al. (2013) proposed to adopt the dynamical mass over the evolutionary mass for  $M_1$ ; i.e., they derived  $M_1 = 14.0 M_{\odot}$  from  $M_1 \sin^3 i = 12.4 M_{\odot}$  and the probable inclination of  $i = 65 - 85$  degree. However, this requires  $\pi$  Aqr to be placed at a 740 pc, which is now unlikely based on the parallax distance measurement with Gaia.

The dynamical solution is also challenged by the recent re-measurement of the radial velocity by Nazé et al. (2019), in which they showed that  $v_1 \sin i$  is only a half of the value by Bjorkman et al. (2002) consistently during 2014–2019. We confirmed this independently in § 3.2. Nazé et al. (2019) also found no evidence of the spectroscopic feature attributable to the secondary unlike the claim by Bjorkman et al. (2002). The phase of the  $\pi$  Aqr was different between Bjorkman et al. (2002) in the normal B phase and Nazé et al. (2019) in the Be phase. They may observe different parts of the system, but the exact cause of the discrepancy is unknown.

We thus deal with the primary mass  $M_1$  as a variable in a reasonable range  $9 - 15 M_{\odot}$  containing both the evolutionary and dynamical estimates. We deal with the radial velocity amplitude  $v_1 \sin i$  fixed to  $8.1 \text{ km s}^{-1}$ , which are confirmed by two independent studies (Nazé et al. 2019 and this work). Then, we can estimate  $M_2$  for a given inclination angle with Kepler's law (figure 8). Bjorkman et al. (2002) discussed that the inclina-

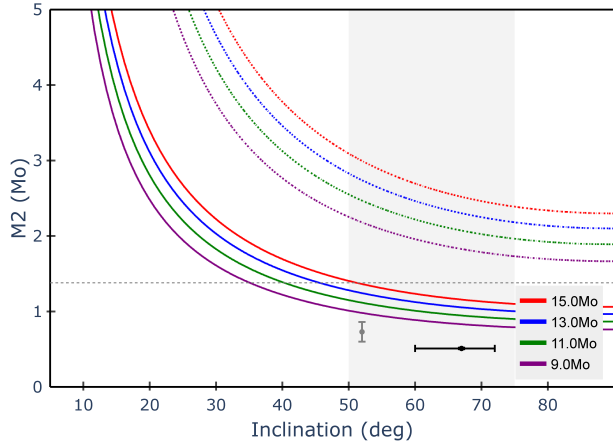


**Fig. 8.** Solution of  $M_2$  as a function of an assumed inclination angle ( $i$ ) for different estimates of  $M_1$  (in different colors) and  $v_1 \sin i = 16.7 \text{ km s}^{-1}$  (dashed curves; Bjorkman et al. 2002) and a half value of it (solid curves; Nazé et al. 2019 and this work). The probable range of the inclination (Bjorkman et al. 2002) is shown in the gray shaded region, while the Chandrasekhar limit for  $M_2$  is by the dotted horizontal line. The best-fit parameters of the magnetic and non-magnetic accreting WD models (tables 2 and 3) are shown with the black and grey points only with statistical errors of the X-ray spectral fitting, respectively.

tion angle should be 50–75 degree because of the large variation of the  $H\alpha$  profile, the double-peaked shape of  $H\beta$  and  $H\gamma$  lines (also seen in figure 6), and a high polarization during the brightness maximum. The  $M_2$  estimate is below the Chandrasekhar limit over an assumed range of the primary mass and the inclination angle.

#### 4.2 Mass estimate with X-ray data

We now compare the revised secondary mass estimate with the X-ray spectral fitting result (§ 3.1). We should note that the application of the WD spectral models to  $\pi$ Aqr is under the working hypothesis that the secondary is a WD. The assumption is validated by the high goodness of the fitting and reasonable values of the best-fit parameters for a WD (tables 2 and 3). We thus use these results.

For the magnetic WD assumption (§ 3.1.2), the spectral model is physically-motivated, thus physical parameters such as  $M_{\text{WD}}$  are available. The model includes the reprocessing components in itself, thus the reflection angle is also constrained as a result of the fitting. We assume that the magnetic pole is aligned to the orbital axis of the binary, thus the X-ray reflection angle ( $i_r$ ) is the same as the orbital inclination. The  $M_2$  and inclination angle are thus constrained by the X-ray spectral fitting alone, which is shown with the black point in figure 8.

For the non-magnetic WD assumption (§ 3.1.1), the spectral model is more phenomenological than the one adopted for the magnetic WD assumption, thus gives less constrained results. Still, we can compare in the  $M_2$  versus inclination angle space

(figure 8). First, it is known that the maximum temperature ( $T_{\text{max}}$ ) is correlated well with  $M_{\text{WD}}$  (figure 9). We derived the linear regression and estimated the range for  $M_2$  based on the  $T_{\text{max}}$  value derived from the fitting to be 0.60–0.86  $M_{\odot}$ . The reflection angle  $i_r = 52$  and 60 degree correspond to an inclination angle of 52 and 75 degree following a simple geometrical argument by Tsujimoto et al. (2018). The result for  $i_r = 60$  degree is shown with the grey data in figure 8.

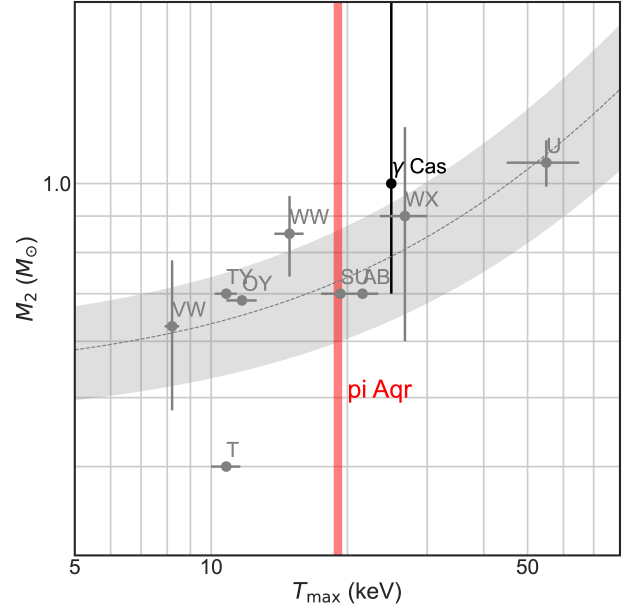


**Fig. 9.** Scatter plot of non-magnetic WD between  $M_2$  by optical spectroscopy versus  $T_{\text{max}}$  by X-ray spectroscopy. Data are from Pandel et al. (2005) for T Leo, OY Car, VW Hyi, WX Hyi, SU UMa, TY, PsA, AB Dra, WW Cet, and U Gem (their abbreviations are given in the figure). For  $\gamma$  Cas, the optical and X-ray results are respectively from Harmanec et al. (2000) and Tsujimoto et al. (2018). For  $\pi$  Aqr, the X-ray result is from table 2 and its  $1\sigma$  range is shown with the red shade. The linear regression of the Pandel et al. (2005) data and its  $1\sigma$  range is shown with the dotted curve and the grey shade.

Whichever the assumption of magnetic or non-magnetic accreting WDs, the X-ray spectral fitting yields a solution in the  $M_2$  versus inclination angle space, which is closer to the optical result adopting the smaller radial velocity amplitude of  $8.1 \text{ km s}^{-1}$ . The WD mass estimate based on the X-ray spectral fitting has systematic uncertainties, which is not shown in figure 8. For the magnetic model, a typical uncertainty is  $\pm 0.2 M_{\odot}$  by comparing the spectroscopic binary mass and the X-ray determined mass using a forerunner model (figure 8 in Yuasa et al. 2010). For the non-magnetic model, we would expect a similar systematic uncertainty from figure 9. The accuracy of the X-ray determined mass in figure 8 is insufficient to discriminate the primary mass (9–15  $M_{\odot}$ ) of the revised radial velocity of  $8.1 \text{ km s}^{-1}$ , but is sufficient to exclude the secondary mass of  $>2.0 M_{\odot}$  previously claimed by Bjorkman et al. (2002) based on the larger radial velocity amplitude of  $16.7 \text{ km s}^{-1}$ .



This puts  $\pi$  Aqr in a comparable range of  $M_2$  estimate among all eight  $\gamma$  Cas analog sources with known spectroscopic binary nature. In Table 4 of Nazé et al. (2022), all  $\gamma$  Cas analog sources have  $M_2 < 1 M_\odot$  except for  $\pi$  Aqr having  $2.4 M_\odot$  based on the Bjorkman et al. (2002) solution. We showed that  $M_2$  estimate for  $\pi$  Aqr should be revised to be lower. We thus conclude that the secondary of  $\pi$  Aqr being a WD is not excluded.

### 4.3 Mass estimate with Gaia

In the Gaia data release latest as of writing (DR3<sup>2</sup>), more than  $8 \times 10^6$  non-single stars are identified either by astrometric (Halbwachs et al. 2022) spectroscopic, or eclipsing methods. We also retrieved the visual binary catalog generated using the early data release of DR3 (El-Badry et al. 2021), but  $\pi$  Aqr was not found either presumably due to the large contrast and small separation between the binary constituents to be detected as a visual binary.

Although  $\pi$  Aqr is not included in the latest Gaia's list of binary stars, the astrometric solution is prospective. For a  $10 M_\odot$  and  $1 M_\odot$  binary with 84.1 day period at a 286 pc away, the semi-major axis of the primary is  $\sim 0.8$  mas. This is within reach of the Gaia's capability (Holl et al. 2022). It is expected that increased data volume and improved algorithms will settle the solution of this source, along with other  $\gamma$  Cas analogs, in the near future.

## 5 Summary & Conclusion

We revisited the secondary mass estimate of  $\pi$  Aqr, which is a  $\gamma$  Cas analog source. In the long-standing debate about the origin of the hard and intense X-ray emission of the  $\gamma$  Cas analog sources,  $\pi$  Aqr plays an important role for being the only two sources of known spectroscopic binary nature along with  $\gamma$  Cas covered for many orbital cycles. The previous estimate of  $M_2$  by Bjorkman et al. (2002) was  $> 2.0 M_\odot$ , which would argue against the idea that the X-ray is produced by accretion onto a WD. However, the mass estimate based on the dynamical solution (Bjorkman et al. 2002) is known to be inconsistent with the evolutionary solution (Zharikov et al. 2013). We obtained new X-ray data using NuSTAR and optical data using OAO HIDES to further investigate this discrepancy.

Our optical spectroscopy shows that the radial velocity amplitude is inconsistent with Bjorkman et al. (2002) and is consistent with Nazé et al. (2019). Based on the revised estimate of the radial velocity amplitude, we constrained  $M_2$  to be below the Chandrasekhar mass limit over an assumed range of the primary mass and the inclination angle.

Independently from this, we conducted spectral fitting of the X-ray data using our NuSTAR and the archived XMM-Newton

data with accreting WD models. This is under the working hypothesis that  $\pi$  Aqr hosts a WD. The assumption is validated by the fact that the fitting yielded high goodness of fit with reasonable best-fit parameters. Separate models for non-magnetic and magnetic WDs were applied and constraints on the  $M_2$  and the inclination angle were obtained. The X-ray results are closer to the optical result adopting the smaller value of the radial velocity amplitude. We thus conclude that the secondary of  $\pi$  Aqr being a WD is not excluded.

We appreciate the support from the staff and volunteers to observe with the OAO 188 cm telescope. We acknowledge Hiroki Harakawa for providing us with the pipeline products of the HIDES data, Yaël Nazé for interesting discussion, and the anonymous reviewer for careful review and correction of critical calculation. This research has made use of the NuSTAR Data Analysis Software (NuSTARDAS) jointly developed by the ASI Space Science Data Center (SSDC, Italy) and the California Institute of Technology (Caltech, USA). This research has made use of the SIMBAD database, operated at CDS, Strasbourg, France and data from from the European Space Agency (ESA) mission *Gaia* (<https://www.cosmos.esa.int/gaia>), processed by the *Gaia* Data Processing and Analysis Consortium (DPAC, <https://www.cosmos.esa.int/web/gaia/dpac/consortium>). Funding for the DPAC has been provided by national institutions, in particular the institutions participating in the *Gaia* Multilateral Agreement.

## References

- Anders, E. & Grevesse, N. 1989, *Geochimica et Cosmochimica Acta*, 53, 197
- Berghoefer, T., Danner, R., & Cassinelli, J. 1997, *A&A*, 322, 167
- Bjorkman, K. S., Miroshnichenko, A. S., McDavid, D., & Pogrosheva, T. M. 2002, *ApJ*, 573, 812
- Brown, A. G. A., Vallenari, A., Prusti, T., et al. 2018, *A&A*, 616, A1
- Ekström, S., Georgy, C., Eggenberger, P., et al. 2012, *A&A*, 537, A146
- El-Badry, K., Rix, H.-W., & Heintz, T. M. 2021, *MNRAS*, 506, 2269
- George, I. M. & Fabian, A. C. 1991, *MNRAS*, 249, 352
- Haberl, F. 1995, *A&A*, 296, 685
- Halbwachs, J.-L., Pourbaix, D., Arenou, F., et al. 2022, *A&A*
- Hamaguchi, K., Oskinova, L., Russell, C. M. P., et al. 2016, *ApJ*, 832, 140
- Harmanec, P., Habuda, P., Stefl, S., et al. 2000, *A&A*, 364, L85
- Harrison, F. A., Craig, W. W., Christensen, F. E., et al. 2013, *ApJ*, 770, 103
- Hayashi, T., Kitaguchi, T., & Ishida, M. 2021, *MNRAS*, 504, 3651
- Holl, B., Sozzetti, A., Sahlmann, J., et al. 2022, *Gaia* DR3 Astrometric Orbit Determination with Markov Chain Monte Carlo and Genetic Algorithms. Systems with Stellar, Substellar, and Planetary Mass Companions
- Jenkins, E. B. 2009, *ApJ*, 700, 1299
- Kambe, E., Yoshida, M., Izumiura, H., et al. 2013, *PASJ*, 65, 15
- Kubo, S., Murakami, T., Ishida, M., & Corbet, R. H. 1998, *PASJ*, 50, 417

<sup>2</sup> See <https://gea.esac.esa.int/archive/documentation/GDR3/>

- Maehara, H. 2013, JSSIJ, 3, 119
- Magdziarz, P., Zdziarski, A. A., Magdziarz Paweł and Zdziarski, A. A., et al. 1995, MNRAS, 273, 837
- Mason, K. O., White, N. E., & Sanford, P. W. 1976, Nature, 260, 690
- Merloni, A., Predehl, P., Becker, W., et al. 2012, arXiv, 1209.3114
- Moritani, Y., Kawano, T., Chimasu, S., et al. 2018, PASJ, 70, 1
- Motch, C., Warwick, R., Cropper, M. S., et al. 2010, A&A, 523, A92
- Mukai, K. 2017, PASP, 129, 062001
- Mushotzky, R. F. & Szymkowiak, A. E. 1988, in Cooling Flows in Clusters and Galaxies, Vol. 229, 53–62
- Nazé, Y., Motch, C., Rauw, G., et al. 2020, MNRAS, 493, 2511
- Nazé, Y., Rauw, G., & Cazorla, C. 2017, A&A, 602, L5
- Nazé, Y., Rauw, G., Czesla, S., Smith, M. A., & Robrade, J. 2022, MNRAS, 510, 2286
- Nazé, Y., Rauw, G., & Smith, M. 2019, A&A, 632, A23
- Pandel, D., Cordova, F. A., Mason, K. O., & Friedhorsky, W. C. 2005, ApJ, 626, 396
- Patterson, J. & Raymond, J. C. 1985, ApJ, 292, 535
- Postnov, K., Oskina, L., & Torrejón, J. M. 2017, MNRAS, 465, L119
- Prusti, T., De Bruijne, J. H. J., Brown, A. G. A., et al. 2016, A&A, 595, A1
- Robinson, R. D. & Smith, M. A. 2000, ApJ, 540, 474
- Shafter, A. W., Szkody, P., & Thorstensen, J. R. 1986, ApJ, 308, 765
- Smith, M. A., Cohen, D. H., Gu, M. F., et al. 2004, ApJ, 600, 972
- Smith, M. A., Lopes de Oliveira, R., & Motch, C. 2016, Advances in Space Research, 58, 782
- Strüder, L., Briel, U., Dennerl, K., et al. 2001, A&A, 365, L18
- Tsujimoto, M., Morihana, K., Hayashi, T., & Kitaguchi, T. 2018, PASJ, 70, 109
- Turner, M. J., Abbey, A., Arnaud, M., et al. 2001, A&A, 365, L27
- Wada, Q., Tsujimoto, M., Ebisawa, K., & Hayashi, T. 2017, PASJ, 69, 1
- White, N. E., Swank, J. H., Holt, S. S., & Parmar, A. N. 1982, ApJ, 263, 277
- Wilms, J., Allen, A., & McCray, R. 2000, ApJ, 542, 914
- Yuasa, T., Nakazawa, K., Makishima, K., et al. 2010, A&A, 520, A25
- Zharikov, S. V., Miroshnichenko, A. S., Pollmann, E., et al. 2013, A&A, 560, A30